Continuous In-Flight Synthesis for On-Demand Delivery of Ligand-Free Colloidal Gold Nanoparticles

Paul Maguire,*,[†][iD] David Rutherford,[†] Manuel Macias-Montero,[†][iD] Charles Mahony,[†] Colin Kelsey,[†] Mark Tweedie,[†] Fátima Pérez-Martin,[†] Harold McQuaid,[†] Declan Diver,[‡] and Davide Mariotti[†]

[†]NIBEC, University of Ulster, Belfast, BT37 0QB, Northern Ireland
[‡]SUPA, School of Physics and Astronomy, University of Glasgow, Glasgow G12 8QQ, United Kingdom

Ⓢ Supporting Information

ABSTRACT: We demonstrate an entirely new method of nanoparticle chemical synthesis based on liquid droplet irradiation with ultralow (<0.1 eV) energy electrons. While nanoparticle formation via high energy radiolysis or transmission electron microscopy-based electron bombardment is well-understood, we have developed a source of electrons with energies close to thermal which leads to a number of important and unique benefits. The charged species, including the growing nanoparticles, are held in an ultrathin surface reaction zone which enables extremely rapid precursor reduction. In a proof-of-principle demonstration, we obtain small-diameter Au nanoparticles (∼4 nm) with tight control of polydispersity, in under 150 μs. The precursor was almost completely reduced in this period, and the resultant nanoparticles were water-soluble and free of surfactant or additional ligand chemistry. Nanoparticle synthesis rates within the droplets were many orders of magnitude greater than equivalent rates reported for radiolysis, electron beam irradiation, or colloidal chemical synthesis where reaction times vary from seconds to hours. In our device, a stream of precursor loaded microdroplets, ∼15 μm in diameter, were transported rapidly through a cold atmospheric pressure plasma with a high charge concentration. A high electron flux, electron and nanoparticle confinement at the surface of the droplet, and the picoliter reactor volume are thought to be responsible for the remarkable enhancement in nanoparticle synthesis rates. While this approach exhibits considerable potential for scale-up of synthesis rates, it also offers the more immediate prospect of continuous on-demand delivery of high-quality nanomaterials directly to their point of use by avoiding the necessity of collection, recovery, and purification. A range of new applications can be envisaged, from theranostics and biomedical imaging in tissue to inline catalyst production for pollution remediation in automobiles.

KEYWORDS: Colloidal nanoparticles, droplet microreactors, segmented flow, plasmas, solvated electron
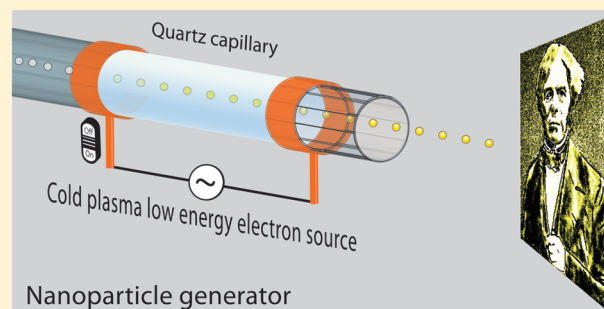
High-quality colloidal nanocrystals play a critical and expanding role in numerous fields including nanomedicine, catalysis, optoelectronics, imaging, and sensors. Control of size, shape, polydispersity, and crystallinity is often a critical requirement. Achieving high production rates and batch-to-batch reproducibility are considered the dominant drivers of new colloidal synthesis chemistries and processes. Chemical synthesis rates are relatively low, and this along with collection and purification stages prevent the direct delivery of as-synthesized nanomaterials to their end-use location on a continuous basis. Such a capability could however transform the use of nanoparticles in that local synthesis, involving high purity and instant delivery, would open up new opportunities and allow for greater flexibility in tailoring the nanoparticle surface yet minimize the threat of agglomeration or the necessity for ligand-based stabilization. New avenues for application that could benefit greatly are, for example, topical, mucosal, or oral drug delivery in nanomedicine,[1−5] wound healing and microbial resistance targeting,[6−8] biodegradable polymer and hydrogel nanocomposites,[9,10] local cell imaging

and biomarker detection,[11] inkjet technologies,[12,13] or continuous airborne catalysis.[14,15] Approaches based on reduced reactor volumes via droplet microfluidics have received attention as a route to continuous and rapid nanomaterial synthesis[16,17] while electron beam techniques, such as TEM in liquid[18,19] and pulse radiolysis, have also shown rapid synthesis capability. However, neither approach offers the practical possibility of direct and continuous nanoparticle delivery.

Atmospheric pressure microplasmas offer opportunities for nanomaterials synthesis in both gas and liquid phases.[20,21] These devices are a rich source of energetic charged and reactive radical species.[22,23] Plasma-based nanoparticle synthesis of various materials has been demonstrated within liquid[24] or at the liquid surface[25] using either suitable electrode materials[26] or liquid precursors.[27] Synthesis times are on the

order of minutes, and stable colloids can be formed without additives. With aqueous precursors, under certain conditions, metal ion reduction is due to reactions with plasma-generated chemical species dissolved from the gas phase, e.g., H_2O_2.[28] Alternatively, energetic electrons from the plasma are known to become solvated[29] at the liquid surface where direct reduction of the metal ions can then occur.[27,30] In this work we have merged the concepts of microfluidics with electron irradiation to create a segmented flow microfluidic device based on metal precursor loaded liquid droplets in a gaseous carrier. Electron irradiation of the droplet surface generates highly reactive solvated electrons as the reducing agent and metal nanoparticles, synthesized instantaneously in flight in the droplet reactor, are carried by the gas flow to their point of use or collection vessel.

Over the past decade, microfluidic approaches to nanoparticle synthesis have received increasing attention in an attempt to achieve continuous synthesis with superior control of size and uniformity.[16,31] The potential for temporal and spatial control offered by microfluidics, along with inline diagnostics, promise opportunities not available to macroscale chemistry and scaling of production rates is an active research topic.[32,33] Microfluidic devices however require complex fabrication steps, can suffer fouling and blockage, and can significantly limit flow rates.[34] Capillary, or millifluidic, devices overcome these issues, but in single phase flow, a wide range of residence times lead to increased dispersion in nanoparticle properties. Mixing times, due to laminar flow, can also be relatively long requiring multilayer 3D mixing structures or coaxial turbulent jets.[17,35] In dual-phase segmented flow schemes, a reactant phase is dispersed in an immiscible carrier fluid leading to discrete isolated microreactor volumes (plugs) each traveling at a constant speed. Plug recirculating flow enhances reactant mixing and temperature equalization,[36] but wall interactions can impact polydispersity and contribute to reactor fouling.[37] With droplet rather than plug flow, the reactant is fully isolated from the wall by the carrier fluid and this approach has demonstrated resilience against reactor fouling. Zhang et al. have demonstrated high production rates in large (mL) droplets in a silicone oil carrier.[33] However, nanoparticle recovery via phase separation can be complex and costly.[38]

Separating the reactant plugs with gas leads to better isolation and enhanced internal plug mixing, while extraction of the final nanoparticle product is also much easier. However, gas flow (bubbles) in microfluidic channels is generally avoided[39] as it can lead to unpredictable liquid flow with long stabilization times and constant manual adjustment.[40] Gunther et al. used a segmented gas–liquid flow to enhance advection and reduce mixing length.[41] Zhang et al. used an air carrier phase for droplet microreactor synthesis of Ag nanoparticles.[42] Apart from facilitating droplet separation, the air also provided oxygen to the reaction and absorbed the gaseous byproducts. Khan et al.[43] reported Au nanoparticle synthesis using an N_2 carrier to allow H_2 out-diffusion. Cabeza et al. observed improvement in Au nanoparticle size and polydispersity using air compared to various liquid carriers.[37]

While chemical synthesis rates are often measured in hours, the need to understand and control the early stage formation of colloidal nanoparticles has led to real-time synchrotron studies,[44−47] with subsecond time-resolution, and the development of new nanoparticle growth models based on a seed–coalescence mechanism.[48] Radiolysis techniques have also been

invaluable in elucidating growth mechanisms, kinetics, and material properties due to well-known reaction rates and controlled input doses (Gy or J kg^{-1}).[49−52] For example, from radiolysis[49] and XPS[53] studies of Au nanoparticle synthesis it is known that metastable intermediate Au^{1+} ions can form via solvated electron reduction of Au^{3+}, which significantly delay nanoparticle synthesis and lead to large size distributions. Kinetic studies of the multistep mechanisms involved in Au^{3+} reduction to $(Au^0)_n$ indicate induction periods of ∼50−100 min, and synthesis via radiolysis occurs on a time scale measured in hours.[49−51,53] However, with pulsed radiolysis, complete reduction of the Au^{3+} ions to Au^0 can occur in a few seconds, provided the dose rates are very high and the initial reduction is rapid across the full reactant volume.[49,54] High-energy electron beam irradiation of liquids in a TEM (through a SiN_4 membrane) produces a much higher electron dose rate, compared to steady-state radiolysis, into femtoliter volumes, and synthesis times on the order of seconds have been reported.[18,19,55,56]

Here we present an entirely new approach involving nanoparticle synthesis on microsecond time scales with the potential for a step change in chemical synthesis capability across a wide range of materials and chemistries. We bring together the concepts of a picoliter droplet microreactor transported in an inert gas carrier phase with low energy electron bombardment of the droplet surface supplying the highly reducing solvated electrons. Precursor loaded micron sized water droplets are transported through a high charge density ($10^{13}−10^{14}$ cm^{-3}) cold atmospheric pressure plasma formed in a 2 mm diameter quartz capillary. The electron dose and growth time scales are determined by local plasma conditions and the droplet time-of-flight through the plasma region, which can be restricted to the microsecond range. No surfactant or ligand chemistry is required to form an electrostatically stable colloidal solution, and nanoparticles can be collected in liquid, on surfaces, or delivered in a pure uncoated state directly to the point of required use, such as biological tissue.

Airborne microdroplets, with a count median diameter of 15 μm, were generated at an average rate of one per 20 μs by a parallel path atomization nebulizer. The droplets were then carried in a three-dimensional coaxial flow along a quartz capillary and through a short (∼2 mm length) high-intensity plasma region, Figure 1. The plasma was created using exterior microelectrodes attached to a high-frequency (13.56 MHz) and high-voltage power source through a custom electrical matching circuit. Details of the experimental setup have already been given previously, and operational parameters are provided in the Supporting Information (SI-1).[57] The device geometry,
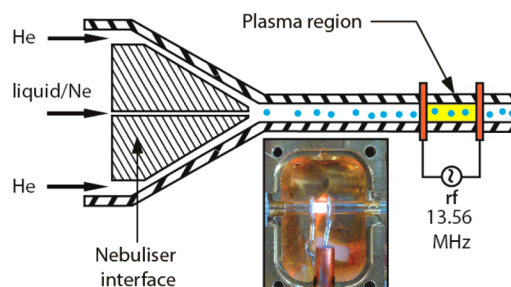

Figure 1. Schematic representation of the droplet–plasma microreactor. (inset) Image of ignited plasma region.

liquid flow, gas flow, and plasma excitation were optimized to obtain laminar noncoalescing droplet flow with minimum droplet diameter and evaporation rate, low gas temperature, and high plasma density.

For an average gas velocity of 17 m s^{-1}, fast, high-resolution imaging confirmed a log-normal droplet size distribution and operation with only a few (∼5) droplets per plasma volume at any instant. The plasma-induced evaporation rate constant was estimated to be 3×10^{-7} m^2 s^{-1} and resulted in a reduction in count median diameter of ∼2 μm (∼30% volume reduction). Only the smaller droplets evaporated totally, resulting in a loss of ∼5% of the total droplet number and ∼0.05% of the total liquid flow volume. The droplet velocities, measured across the capillary diameter, followed a parabolic velocity envelope consistent with near laminar gas flow within the quartz tube. The median time-of-flight through the plasma region is ∼120 μs, as measured outside the quartz tube, although turbulence and drag is likely to have slowed the droplets somewhat. Net RF power into the plasma was measured using a close-coupled inline VI diagnostic probe (Impedans Octiv Suite) after subtraction of measured cable and system impedance without plasma ignited. The power deposited into the plasma volume is in the range 0.3−0.4 W, and the introduction of droplets requires no additional power, indicating the droplets have little effect on the plasma and the droplet charge is a negligible fraction of the total volumetric charge.

For Au nanoparticle (NP) formation in-flight, a gold(III) chloride trihydrate (HAuCl$_4$·3H$_2$O) aqueous solution (1.0 mM HAuCl$_4$ concentration, pH 4) was made up from a solid powder (Sigma-Aldrich, UK) and supplied to the nebulizer. Indicator strips were placed at the right end exit of the capillary (see Figure 1) to evaluate the pH of the droplets after exposure to the plasma, and these showed no significant change in pH. In the same way, the plasma treated droplets were also collected, for 30 s, on TEM grids located 20 mm downstream of the plasma region. Control grids exposed to the plasma without droplets or to nonplasma treated droplets showed no nanoparticle formation. From TEM analysis we observe the formation of high-quality crystalline Au nanoparticles (NPs) after plasma irradiation with a log-normal size distribution of 4.4 nm count median diameter and a narrow polydispersity (geometric standard deviation 1.5), shown in Figure 2.

Estimates of precursor reduction and nanoparticle concentration were obtained from ultraviolet/visible (UV−vis) spectra in the range 200−300 nm where precursor absorption is dominant. While the small sample volume and the dilution during collection limit the accuracy of these techniques, we estimate that >50% of the HAuCl$_4$ precursor is reduced during the plasma exposure (see Supporting Information, SI-2).

It is known that nanoparticle formation is possible from a vaporised liquid precursor or colloid[58] injected into a furnace[59] or hot gas plasma[60] or through the use of electrospray charged droplets.[61] With these approaches, synthesis relies on the total evaporation of the carrier solvent. However, in our case, the gas remains below ∼360 K,[57] and only a small volume fraction (∼0.05%) of the droplets evaporate completely in flight. Thus, the droplet acts as a true reactor vessel whereby metal ions are reduced due to surface electron irradiation and the internal droplet diffusion and recirculation promotes transport and mixing of reactant. We observe a fully developed nanoparticle distribution for synthesis times ∼120 μs, many orders of magnitude faster than reported for conventional colloidal chemistry routes. We have previously demonstrated Au NP
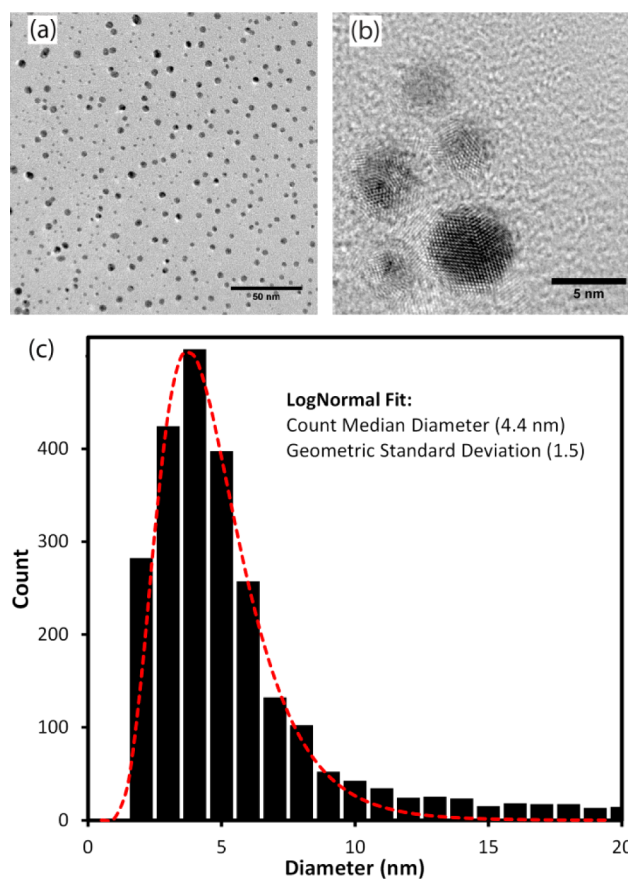
Figure 2. TEM images of (a) Au NPs deposited onto grid direct from plasma, (b) a typical nanoparticle with diameter 4.5 nm, and (c) the particle size distribution, obtained from a sample of 2100 nano-particles, showing a mean diameter of 4.4 nm.

synthesis in bulk liquid via surface plasma bombardment of the liquid for 10 min.[25] This resulted in a much larger average NP diameter (200 nm, σ = 40 nm) at the 1 mM precursor concentration, while small nanoparticles (6 nm, σ = 1 nm) were obtainable at 0.01 mM. In this case, reduction of the HAuCl$_4$ precursor by plasma generated H$_2$O$_2$ was considered the most likely mechanism leading to nanoparticle synthesis. The kinetics of direct H$_2$O$_2$ reduction of precursor indicate a first-order reduction rate constant of 5×10^{-3} s^{-1} for high concentration H$_2$O$_2$ (6.7 M) (see Supporting Information SI-2). Similar mechanisms have been reported for other plasma configurations in contact with bulk liquid, and similar time scales for direct H$_2$O$_2$ reduction of HAuCl$_4$ precursor have also been reported in the literature.[23,62,63] However, with plasma−droplet synthesis, the maximum time-of-flight between plasma and TEM collection grid is 10^{-3} s, and since H$_2$O$_2$ reduction of the precursor occurs on a time scale of minutes, it is therefore not thought to be significant in this case.

For a 1 mM HAuCl$_4$ precursor concentration with 50% reduction over a ∼120 μs exposure time for each droplet, the conversion rate of Au^{3+} to Au^0 metal atoms that contribute to NP growth is $>10^{24}$ atoms s^{-1} L^{-1}, as in Figure 3. This represents a figure of merit for the NP synthesis rate and is significantly higher, by many orders of magnitude, than the equivalent observed with traditional colloidal chemistry processes.

Detailed kinetic studies via XANES and SAXS indicate a conversion rate of 10^{18} atoms s^{-1} L^{-1} for the standard
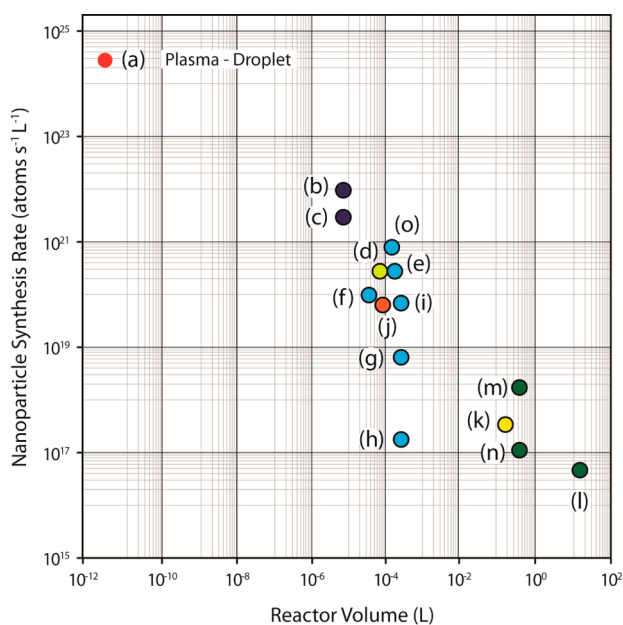
Figure 3. (a) Nanoparticle synthesis rate of plasma-exposed droplets, determined from the rate of reduction of HAuCl4, compared with equivalent rates extracted from published literature for different reactor architectures and volumes, namely, (b and c) microfluidic reactors, (d) turbulent capillary flow device, (e–i and o) stopped or continuous flow devices, (j) gas-segmented flow device, (k) laminar capillary flow device, and (l–n) batch reactor processes. Literature reference details are given in Supporting Information SI-3.

Turkevich process[64,65] and 10^{20} atoms s^{-1} L^{-1} for NP growth based on monophasic TBAB reduction in a stopped-flow reactor.[46,66] Other kinetic studies utilizing stopped or continuous flow mixers and a selection of chemistries indicate conversion rates between 10^{16} and 10^{20} atoms s^{-1} L^{-1}. Millifluidic and microreactor synthesis using strong ($NaBH_4$) reducing agents have been reported, and estimates of conversion rates have been extracted from experimental details. For laminar flow millifluidic tubing with a reaction volume of ~150 mL, Lohse et al.[67] reported the equivalent of >10^{17} atoms s^{-1} L^{-1}, while Sebastian Cabeza et al.[37] achieved >10^{19} atoms s^{-1} L^{-1} in a 100 μL segmented flow device using air bubbles in an aqueous carrier. For a similar reaction volume (~90 μL) but with turbulent mixing, Han et al. obtained >10^{20} atoms s^{-1} L^{-1} using ascorbic acid as a reducing agent.[68] In microfluidic devices with much smaller reaction volumes (~8 μL) the equivalent of >5×10^{20} atoms s^{-1} L^{-1} and ~10^{22} atoms s^{-1} L^{-1} are achievable for $NaBH_4$ and ascorbic acid reducing agents, respectively[31,69] (see Supporting Information, SI–3). This tentative inverse correlation between reactor volume and conversion rate is not surprising, and hence the greatly enhanced conversion rate observed with isolated picolitre droplets can be partly attributed to the very rapid mixing capability afforded by such small volumes. However, the possible presence of solvated electrons, one of the strongest reducing agents available, due to the electron irradiation can be expected to also play a significant role.

Solvated electron reduction of Au precursor is well-understood from radiation chemistry where the formation of intermediate metastable species are known to delay nanoparticle formation and large size distributions result.[49] Kinetic studies of the multistep mechanisms involved in Au^{3+} reduction to (Au^0)$_n$ indicate induction periods of ~50−100 min which

can in part be accounted for by disproportionation of Au^{2+} into Au^{3+}/Au^{1+} and by the comproportionation of Au^0 with Au^{3+} into Au^{2+}/Au^{1+}.[49,51,53] At very high dose rates, however, complete reduction to Au^0 can be achieved before stabilization of these intermediate species occurs. High-energy electron beam irradiation of liquids in a TEM (through a SiN$_4$ membrane) produces a much higher electron dose rate compared to radiolysis, and the dose is deposited into femtoliter volumes with a corresponding greater yield of reaction products.[18,19,55,56] Nanoparticle synthesis time scales are reduced from hours to minutes or even seconds under these high-dose, high-energy irradiation conditions, compared to steady-state radiolysis. By comparison with the droplet case, the equivalent electron dose rate (i.e., J kg^{-1} s^{-1}) is much lower, as is the irradiation energy thus allowing exploration of a hitherto inaccessible parameter space.

The radio frequency voltage excitation of the confined gas volume creates a non(thermal) equilibrium plasma where the average electron energy is much greater than that of the ions, which remain at a similar temperature to the cool gas. The plasma region contains a high density of charged particles with equal numbers of positive ions and electrons. On entering the plasma, a droplet will acquire a net negative charge due to the much higher mobility of bombarding electrons compared to ions. A negative floating potential is then established on the droplet within the ion plasma period (~10 ns), and thereafter the ion and electron fluxes are equal. A thin electric field (sheath) region, depleted of electrons, is set up around the droplet, and only the higher energy electrons in the plasma, capable of overcoming the floating potential, are now able to reach the droplet. Given the typical electron energy distribution within the plasma, electrons can be expected arrive at the droplet surface with energies close to the floating potential, i.e., almost zero net energy. Positive ions are however accelerated by the electric field in the sheath region, and their arrival energy will depend on collisions with neutral gas atoms en route and the electric field gradient. Charged particle fluxes, particularly electrons, interact with Au complexes in the droplet causing reduction via a number of chemical pathways. Competing reactions such as H_2O dissociation in the liquid phase[70,71] as well as H_3O^+ formation in the vapor phase are also known to occur.[72,73]

In order to compare the nanoparticle formation rates in the plasma−aerosol microreactor with those of radiolysis and electron-beam irradiation, we determine an equivalent plasma dose rate from an estimate of the energy input per droplet. The measured power deposited into the plasma volume is 0.3−0.4 W. By making the assumption that power is delivered uniformly throughout the plasma volume we estimate, from the plasma−droplet volume ratio, the power received by each droplet is ~0.1 μW.

For a flight time through the plasma of 120 μs, this is equivalent to a dose rate of ~10^{-2} kGy s^{-1}, (J kg^{-1} s^{-1}) which is of similar magnitude to the low rates used in gamma radiolysis but much less than that obtained with high-energy electron beam irradiation of liquid (at 300 kV). Nevertheless, the plasma-induced reduction of Au^{3+} and the formation of Au^0 in nanoparticles proceeds at a rate that is ~10^3 times greater than the fastest rates previously observed with high dose rate TEM and over 10^7 faster than gamma radiolysis, for similar dose rates, Figure 4 (see Supporting Information, SI-3). Such a remarkable enhancement of the reaction efficiency must depend on factors in addition to that of reduced volume,
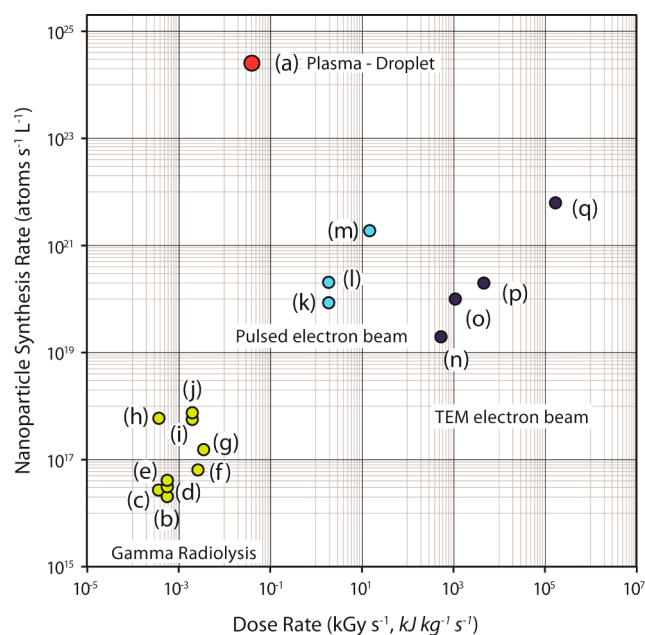
Figure 4. (a) Nanoparticle synthesis rate against dose rates of plasma-exposed droplets, determined from the rate of reduction of $HAuCl_4$, compared with equivalent rates extracted from published literature for (b–j) steady-state gamma radiolysis, (k–m) pulsed electron beam, and (n–q) high dose rate TEM electron beam into the liquid cell. The dose rate is calculated from the measured power deposited into the plasma times the ratio of droplet to plasma volume. Literature reference details are given in Supporting Information SI-3.

since extremely small volumes are used in the TEM studies. Gamma radiolysis (and electron beam irradiation) produces energy loss events in isolated and localized spurs. These spurs contain most of the generated species, and the yields of electron scavengers (OH and H^+) are similar to that of solvated electrons (e_{aq}^-).[49] The availability of the latter for gold reduction is therefore considerably limited by scavenging reactions within the spur. Hydroxylation of the Au complexes in the region of the spur also lowers the redox potential of the complex.[48] In the plasma case, the droplet surface is irradiated by low energy positive ions and electrons. The droplet in the plasma is at a negative floating potential which repels electrons, and only those with sufficient energy can reach the surface. The electron concentration versus energy distribution in such a nonequilibrium plasma follows an exponential reduction with increasing energy. Therefore, we can state with confidence that the net arrival energy of the electrons is almost zero. Electron interactions with water molecules in the vapor phase around the droplet may also produce additional gas species, mainly HeH^+, He^*, H_3O^+, OH^+, H^+, H_2^+, O^+, OH, H, H_2, and O at high electron energy and OH^-, O^-, and H^- by attachment at lower energy. Generated gas species such as H_2O_2 and OH can then dissolve into the liquid and may act as electron scavengers.[74,75]

The charge flux to the droplet is an important parameter in determining the supply rate of electrons for precursor reactions. However, for collisional plasma conditions, there are no experimental comparisons and theoretical understanding is limited. It is likely that the flux is strongly dependent on plasma charge concentration and plasma electron energy distribution. We have measured charge concentrations >10^{20} m^{-3} in a similar plasma configuration operated with Ar/SiH_4 and without

liquid.[76] This value of charge concentration is significantly greater than that obtainable from corona discharge or electrospray charging of droplets. Using the simulation outputs of a collisional plasma model by Patacchini and Hutchinson,[77] we estimate an electron flux density in the range 10^{22}–10^{25} m^{-2} s^{-1} for droplets of mean diameter ∼15 μm and plasma charge concentrations between 10^{19}–10^{22} m^{-3}. At this level of flux density, the net droplet surface charge is estimated to be 10^5–10^6 electrons.

Hot electrons reaching a water surface rapidly equilibrate when the delocalized quasi-free electron becomes localized or prehydrated and then ultimately solvated (hydrated), within a subpicosecond time scale.[78] Electrons will then react with species including H_2O^+, H_3O^+, O, H, O_2, OH, and H_2O_2 with rate constants >10^{10} M^{-1} s^{-1}. The second-order dielectron[79] reaction (1) with a rate constant[80] $2k = 1.1 \times 10^{10}$ M^{-1} s^{-1} may also be important.

The reaction−diffusion penetration depth is estimated to be ∼4 nm from the reaction half-life (bulk) and the solvated electron diffusion constant (4.9×10^{-8} m^2 s^{-1}). This leads to estimates of surface electron concentrations between 0.7 mM and 70 mM over the range of flux densities estimated above. Park et al.[18] have observed an effective reduction rate of ∼10^{-4} atoms per beam electron (Au^0/e^-) in TEM studies where production rates of electron scavengers (H^+, OH^-) are similar to that of the electrons. Their reaction−diffusion model provides an estimate of steady-state hydrated electron concentration between 10^{-7} M and 10^{-5} M with a beam electron flux density of ∼10^{22} m^{-2} s^{-1}. For the same value of plasma electron flux density, the effective reduction rate is 10^0 Au^0/e^-, and complete reduction would occur over the droplet flight time. At 10^{26} m^{-2} s^{-1} the complete reduction time would be reduced to ∼13 ns. However, in the plasma case, the electrons arriving at the droplet have approximately thermal energy and the interaction of such low energy electrons with liquid water has not previously been studied. Also the supply of precursor from the interior to the surface may be a limiting factor.

The hydration of an electron requires the breaking of many H-bonds (0.1 eV each) and the reorientation of water molecules to form the cavity.[81] An important question therefore is whether a low energy electron becomes hydrated or remains confined at the surface. Simulations of water clusters present a conflicting picture where in some cases electron binding to the surface was found to be feasible,[82−84] while other simulations indicate that an electron added to a neutral water surface spontaneously forms a fully hydrated species.[85] Rumbach et al.[29] have measured the hydrated electron absorption spectra at a plasma−liquid film interface and determined a penetration depth of 2.5 nm, concluding therefore that full solvation occurs. From this, they estimated the surface electron concentration at ∼1 mM for an electron flux of 10^{23} m^{-2} s^{-1}. Sagar et al.[86] generated electrons at the water−air interface via a charge transfer to solvent (CTTS) mechanism and observed electron localization at depths of ∼1 nm, i.e., near-surface but fully hydrated. Since the electrons are generated by UV excitation of the anion CTTS band, the initial electron energy (∼ few eV) is a possible factor in the hydration mechanism. Recently Siefermann et al.[87,88] determined experimentally, from photoelectron spectra, vertical binding energies of 1.6 and 3.6 eV for surface and bulk hydrated electrons in water, respectively. It was found that surface electrons were relatively stable with lifetimes much longer than

expected from theory, and it was concluded that a significant free-energy barrier, estimated to be between 0.2 and 0.5 eV, exists between surface and bulk hydration of the hydrated electron in water. Finally, models of additional radiation absorption by weakly charged raindrops indicate free electrons are bound to the surface in quantized confining potentials with a band transition threshold of ~0.64 eV.[89]

Whether the surface concentration of electrons is determined by standard reaction−diffusion, electrostatic confinement or by additional surface energy barriers, it is evident that nanoparticle formation in the droplet is a surface driven process and therefore advection of precursor from the interior to the surface is required. Further, it is also possible that nanoparticles remain at the surface during growth. According to recent understanding of NP growth,[48,90] the number of NPs generated at the initial stage is determined by the amount of available Au^0 from the initial reduction and the optimum NP size (typically ~1 nm) due to colloidal stability (a balance between van der Waals attractive forces and electric double layer repulsion). These form the seed particles for subsequent growth. The maximum number of nanoparticles with a mean diameter of 4.4 nm that can be generated in a droplet with 1 mM precursor is 3 × 10^5. Since the droplet on entering the plasma is uncharged, the initial electron flux is much higher than the steady-state value and if, as theory suggests, the number of initially formed seed particles at the surface establishes the final NP count, then the average distance between seeds is ~44 nm. Under steady-state conditions the average distance between free electrons varies from 160 to 60 nm for electron fluxes between 10^{22} m^{-2} s^{-1} and 10^{26} m^{-2} s^{-1}, while that between Au^{3+} ion complexes at the surface is 22 nm. Furthermore, experiments and simulations have indicated a strong surface propensity of halide ions in aqueous solutions.[91] Therefore, the average distance between an arriving electron and either a nanoparticle or an Au^{3+} ion is 16 and 9 nm respectively for a flux value of 10^{26} m^{-2} s^{-1}. The equivalent electron diffusion times are 1.3 and 0.4 ns compared to that of the electron−electron at 22 ns.[92] Therefore, unlike the bulk liquid case, the dielectron reaction (1) need not be dominant provided precursor supply to the surface is not the limiting factor. Diffusion times for Au^{3+} ions from center to droplet surface are similar to the plasma flight time. Although scavenging of electrons by H^+ may be important, the plasma is also a source of gaseous H_2O_2 which dissolves in the droplet. The measured average droplet concentration was 10 mM. However, an enhanced surface H_2O_2 concentration up to ~0.46 M is feasible (see Supporting Information SI-2). Under these conditions the reactions $e_{aq}^- + H_2O_2 \rightarrow OH + OH^-$ and $e_{aq}^- + OH \rightarrow OH^-$ would dominate over Au^{3+} reduction. Increasing the probability of the latter requires high electron fluxes and droplet mixing, in order to bring precursor to the surface and to diminish the surface H_2O_2 concentration. In addition, autocatalytic reduction of precursor by the growing nanoparticles, acting as seeds, is well-known. Droplet mixing by internal convection requires a difference between droplet and local gas speed. Measured droplets velocities are ~75% of the local gas velocity resulting in a high liquid Péclet number, and hence the probability of rapid mixing is high. Diffusion of the seed or the growing nanoparticles out of the surface reaction zone proceeds at a much slower rate; a 5−10 nm NP will travel about 2% of the droplet radius during the plasma flight time. Also, it has recently been observed that Au NPs can be very efficient ultrafast scavengers of electrons, and in this eventuality,

diffusion of the charged nanoparticles into the droplet would be restricted due to electrostatic considerations.[93]

The reduction mechanisms of $HAuCl_4$, while complex, have been studied extensively by radiolytic and other methods. The solvated electron is known to be one of the strongest/fastest reducing agents. However, the reduction of the Au^{3+}−chloride complex to a Au^0 - chloride complex is nonlinear and involves intermediate Au^{2+} and Au^{1+} species which are long-lived. Park et al.,[18] in TEM studies, observed no Au crystals until the liquid was irradiated with almost half the dose required for the total reduction of Au^{3+} to Au^0. This delay time increases quadratically with the liquid volume.[56] Overcoming the intermediate Au^{1+} reduction delay requires sufficient reductant to satisfy the competition between Au^{3+} and Au^{1+} electron reactions and maintain a near unity Au^{3+}/Au^{1+} ratio. Alternatively Au^{1+} species will reduce rapidly at a NP surface leading to growth. Confinement of the reaction to the droplet surface may enhance the concentration of both electrons and nanoparticles sufficiently to enable the very high reduction rates observed.

In summary, the nanoparticle formation rate in the plasma−droplet system surpasses by many orders of magnitude that obtained by batch and microreaction chemistry, radiolysis, or high energy electron irradiation approaches. The reduced volume of the droplet microreactor is insufficient to explain this remarkable rate enhancement. However, confinement of the reaction to the surface further constrains the volume. While the exact electron flux to the droplet is not known, it is likely that effective surface electron concentrations are sufficiently high to accommodate competing reactions with, for example, plasma generated H_2O_2. With sufficient local oversupply of electrons to meet the needs of Au^{3+} reduction, the normally long delay in Au^{1+} reduction can be avoided. Internal droplet advection is required to transport precursor complexes to the surface while also diminishing possible surface concentration gradients of competing species dissolved from the gas phase. Seed nanoparticle formation at the surface and nanoparticle trapping due to electron capture would also provide valuable local catalyst sites for rapid Au^{1+} reduction.[93]

Plasma droplet synthesis of small spherical Au nanoparticles has been demonstrated. The future development of this approach for size, shape, and facet control is possible through control of electron flux, gas chemistry, and residence time in the plasma while precursor concentration and the use of additional chemistries, such as $Ag^+/CTAB$ and $Cu^{2+}/CTAB$, already established in colloidal NP synthesis, offer an unchartered expanse for further exploration. Successful plasma−droplet nanoparticle synthesis opens new opportunities for one-step synthesis and direct delivery of nanomaterials in applications from gas-phase catalysis to wound healing and cancer theranostics. Additionally the capability of producing such low energy electron interactions with liquid may have important implications for the study of low-energy electron cancer therapy,[94] hydrogen generation by radiochemical/catalytic methods, and nuclear waste management.[95]

■ ASSOCIATED CONTENT

ⓢ Supporting Information

The Supporting Information is available free of charge on the ACS Publications website at DOI: 10.1021/acs.nanolett.6b03440.

Plasma setup and methods along with droplet velocity and size characterization. Additional TEM figures. UV

absorbance spectra. Precursor reduction and nanoparticle synthesis rates comparison (PDF)

■ AUTHOR INFORMATION

Corresponding Author
*E-mail: pd.maguire@ulster.ac.uk.

ORCID
Paul Maguire: 0000-0002-2725-4647
Manuel Macias-Montero: 0000-0002-5508-928X

Notes
The authors declare no competing financial interest.

■ REFERENCES

(1) Wilhelm, S.; Tavares, A. J.; Dai, Q.; Ohta, S.; Audet, J.; Dvorak, H. F.; Chan, W. C. W. *Nature Rev. Mater.* **2016**, *1*, 16014.
(2) Kaushik, N. K.; Kaushik, N.; Yoo, K. C.; Uddin, N.; Kim, J. S.; Lee, S. J.; Choi, E. H. *Biomaterials* **2016**, *87*, 118−130.
(3) Cario, E. *Mucosal Immunol.* **2012**, *5*, 2−3.
(4) Fromen, C. A.; Robbins, G. R.; Shen, T. W.; Kai, M. P.; Ting, J. P. Y.; DeSimone, J. M. *Proc. Natl. Acad. Sci. U. S. A.* **2015**, *112*, 488−493.
(5) Praetorius, N. P.; Mandal, T. K. *J. Pharm. Pharmacol.* **2008**, *60*, 809−815.
(6) Besinis, A.; De Peralta, T.; Tredwin, C. J.; Handy, R. D. *ACS Nano* **2015**, *9*, 2255−2289.
(7) Ortiz-Benitez, E. A.; Carrillo-Morales, M.; Velazquez-Guadarrama, N.; Fandino-Armas, J.; Olivares-Trejo, J. *Metallomics* **2015**, *7*, 1173−1179.
(8) Lemire, J. A.; Harrison, J. J.; Turner, R. J. *Nat. Rev. Microbiol.* **2013**, *11*, 371−384.
(9) GhavamiNejad, A.; Park, C. H.; Kim, C. S. *Biomacromolecules* **2016**, *17*, 1213−1223.
(10) Meyer, R. A.; Green, J. J. *Nanomedicine (London, U. K.)* **2015**, *10*, 3421−3425.
(11) Chinen, A. B.; Guan, C. M.; Ferrer, J. R.; Barnaby, S. N.; Merkel, T. J.; Mirkin, C. A. *Chem. Rev.* **2015**, *115*, 10530−10574.
(12) Secor, E. B.; Ahn, B. Y.; Gao, T. Z.; Lewis, J. A.; Hersam, M. C. *Adv. Mater.* **2015**, *27*, 6683−6688.
(13) Han, Y. L.; Hu, J.; Genin, G. M.; Lu, T. J.; Xu, F. *Sci. Rep.* **2014**, *4*, 4872.
(14) Astruc, D.; Lu, F.; Aranzaes, J. R. *Angew. Chem., Int. Ed.* **2005**, *44*, 7852−7872.
(15) Gavia, D. J.; Shon, Y. *ChemCatChem* **2015**, *7*, 892−900.
(16) Zhang, L.; Xia, Y. *Adv. Mater.* **2014**, *26*, 2600−2606.
(17) Liu, D.; Cito, S.; Zhang, Y.; Wang, C.-F.; Sikanen, T. M.; Santos, H. A. *Adv. Mater.* **2015**, *27*, 2298−2304.
(18) Park, J. H.; Schneider, N. M.; Grogan, J. M.; Reuter, M. C.; Bau, H. H.; Kodambaka, S.; Ross, F. M. *Nano Lett.* **2015**, *15*, 5314−5320.
(19) Alloyeau, D.; Dachraoui, W.; Javed, Y.; Belkahla, H.; Wang, G.; Lecoq, H.; Ammar, S.; Ersen, O.; Wisnet, A.; Gazeau, F.; Ricolleau, C. *Nano Lett.* **2015**, *15*, 2574−2581.
(20) Askari, S.; Svrcek, V.; Maguire, P.; Mariotti, D. *Adv. Mater.* **2015**, *27*, 8011−8016.
(21) Ghosh, S.; Bishop, B.; Morrison, I.; Akolkar, R.; Scherson, D.; Mohan Sankaran, R. *J. Vac. Sci. Technol., A* **2015**, *33*, 021312.
(22) Mariotti, D.; Sankaran, R. M. *J. Phys. D: Appl. Phys.* **2010**, *43*, 323001.
(23) Chen, Q.; Kaneko, T.; Hatakeyama, R. *Appl. Phys. Express* **2012**, *5*, 086201.

(24) Sudare, T.; Ueno, T.; Watthanaphanit, A.; Saito, N. *Phys. Chem. Chem. Phys.* **2015**, *17*, 30255−30259.
(25) Mariotti, D.; Patel, J.; Švrček, V.; Maguire, P. *Plasma Processes Polym.* **2012**, *9*, 1074−1085.
(26) Belmonte, T.; Hamdan, A.; Kosior, F.; Noel, C.; Henrion, G. *J. Phys. D: Appl. Phys.* **2014**, *47*, 224016.
(27) Richmonds, C.; Sankaran, R. M. *Appl. Phys. Lett.* **2008**, *93*, 131501.
(28) Patel, J.; Němcová, L.; Maguire, P.; Graham, W. G.; Mariotti, D. *Nanotechnology* **2013**, *24*, 245604.
(29) Rumbach, P.; Bartels, D. M.; Sankaran, R. M.; Go, D. B. *Nat. Commun.* **2015**, *6*, 7248.
(30) Richmonds, C.; Witzke, M.; Bartling, B.; Lee, S. W.; Wainright, J.; Liu, C. C.; Sankaran, R. M. *J. Am. Chem. Soc.* **2011**, *133*, 17582−17585.
(31) Wagner, J.; Köhler, J. M. *Nano Lett.* **2005**, *5*, 685−691.
(32) Phillips, T. W.; Lignos, I. G.; Maceiczyk, R. M.; deMello, A. J.; deMello, J. C. *Lab Chip* **2014**, *14*, 3172−3180.
(33) Zhang, L.; Niu, G.; Lu, N.; Wang, J.; Tong, L.; Wang, L.; Kim, M. J.; Xia, Y. *Nano Lett.* **2014**, *14*, 6626−6631.
(34) Riche, C. T.; Roberts, E. J.; Gupta, M.; Brutchey, R. L.; Malmstadt, N. *Nat. Commun.* **2016**, *7*, 10780.
(35) Lim, J. -M.; Swami, A.; Gilson, L. M.; Chopra, S.; Choi, S.; Wu, J.; Langer, R.; Karnik, R.; Farokhzad, O. C. *ACS Nano* **2014**, *8*, 6056−6065.
(36) Lee, S.; Gallaire, F.; Baroud, C. N. *Soft Matter* **2012**, *8*, 10750−10758.
(37) Sebastian Cabeza, V.; Kuhn, S.; Kulkarni, A. A.; Jensen, K. F. *Langmuir* **2012**, *28*, 7007−7013.
(38) Zhang, L.; Wang, Y.; Tong, L.; Xia, Y. *Nano Lett.* **2014**, *14*, 4189−4194.
(39) Lochovsky, C.; Yasotharan, S.; Günther, A. *Lab Chip* **2012**, *12*, 595−601.
(40) Abolhasani, M.; Singh, M.; Kumacheva, E.; Günther, A. *Lab Chip* **2012**, *12*, 4787−4795.
(41) Günther, A.; Jhunjhunwala, M.; Thalmann, M.; Schmidt, M. A.; Jensen, K. F. *Langmuir* **2005**, *21*, 1547−1555.
(42) Zhang, L.; Wang, Y.; Tong, L.; Xia, Y. *Langmuir* **2013**, *29*, 15719−15725.
(43) Khan, S. A.; Duraiswamy, S. *Lab Chip* **2012**, *12*, 1807−1812.
(44) Li, T.; Senesi, A. J.; Lee, B. *Chem. Rev.* **2016**, *116*, 11128−11180.
(45) Abecassis, B.; Bouet, C.; Garnero, C.; Constantin, D.; Lequeux, N.; Ithurria, S.; Dubertret, B.; Pauw, B. R.; Pontoni, D. *Nano Lett.* **2015**, *15*, 2620−2626.
(46) Abécassis, B.; Testard, F.; Kong, Q.; Francois, B.; Spalla, O. *Langmuir* **2010**, *26*, 13847−13854.
(47) Polte, J.; Erler, R.; Thünemann, A. F.; Sokolov, S.; Ahner, T. T.; Rademann, K.; Emmerling, F.; Kraehnert, R. *ACS Nano* **2010**, *4*, 1076−1082.
(48) Wuithschick, M.; Birnbaum, A.; Witte, S.; Sztucki, M.; Vainio, U.; Pinna, N.; Rademann, K.; Emmerling, F.; Kraehnert, R.; Polte, J. *ACS Nano* **2015**, *9*, 7052−7071.
(49) Gachard, E.; Remita, H.; Khatouri, J.; Keita, B.; Nadjo, L.; Belloni, J. *New J. Chem.* **1998**, *22*, 1257−1265.
(50) Dey, G. R.; El Omar, A. K.; Jacob, J. A.; Mostafavi, M.; Belloni, J. *J. Phys. Chem. A* **2011**, *115*, 383−391.
(51) Dey, G. R. *Radiat. Phys. Chem.* **2014**, *102*, 44−48.
(52) Henglein, A.; Meisel, D. *Langmuir* **1998**, *14*, 7392−7396.
(53) Fong, Y. -Y.; Visser, B. R.; Gascooke, J. R.; Cowie, B. C. C.; Thomsen, L.; Metha, G. F.; Buntine, M. A.; Harris, H. H. *Langmuir* **2011**, *27*, 8099−8104.
(54) Hanžić, N.; Jurkin, T.; Maksimović, A.; Gotić, M. *Radiat. Phys. Chem.* **2015**, *106*, 77−82.
(55) Grogan, J. M.; Schneider, N. M.; Ross, F. M.; Bau, H. H. *Nano Lett.* **2014**, *14*, 359−364.
(56) Schneider, N. M.; Norton, M. M.; Mendel, B. J.; Grogan, J. M.; Ross, F. M.; Bau, H. H. *J. Phys. Chem. C* **2014**, *118*, 22373−22382.
(57) Maguire, P. D.; Mahony, C. M. O.; Kelsey, C. P.; Bingham, A. J.; Montgomery, E. P.; Bennet, E. D.; Potts, H. E.; Rutherford, D. C. E.;

McDowell, D. A.; Diver, D. A.; Mariotti, D. *Appl. Phys. Lett.* **2015**, *106*, 224101.

(58) Dhand, C.; Dwivedi, N.; Loh, X. J.; Jie Ying, A. N.; Verma, N. K.; Beuerman, R. W.; Lakshminarayanan, R.; Ramakrishna, S. *RSC Adv.* **2015**, *5*, 105003−105037.

(59) Swihart, M. T. *Curr. Opin. Colloid Interface Sci.* **2003**, *8*, 127−133.

(60) Marchand, C.; Chazelas, C.; Mariaux, G.; Vardelle, A. *J. Therm. Spray Technol.* **2007**, *16*, 705−712.

(61) Suhendi, A.; Nandiyanto, A. B. D.; Munir, M. M.; Ogi, T.; Gradon, L.; Okuyama, K. *Langmuir* **2013**, *29*, 13152−13161.

(62) Paclawski, K.; Fitzner, K. *Metall. Mater. Trans. B* **2006**, *37*, 703−714.

(63) Liu, X.; Xu, H.; Xia, H.; Wang, D. *Langmuir* **2012**, *28*, 13720−13726.

(64) Polte, J.; Ahner, T. T.; Delissen, F.; Sokolov, S.; Emmerling, F.; Thünemann, A. F.; Kraehnert, R. *J. Am. Chem. Soc.* **2010**, *132*, 1296−1301.

(65) Polte, J.; Erler, R.; Thünemann, A. F.; Emmerling, F.; Kraehnert, R. *Chem. Commun.* **2010**, *46*, 9209−9211.

(66) Abécassis, B.; Testard, F.; Spalla, O.; Barboux, P. *Nano Lett.* **2007**, *7*, 1723−1727.

(67) Lohse, S. E.; Eller, J. R.; Sivapalan, S. T.; Plews, M. R.; Murphy, C. J. *ACS Nano* **2013**, *7*, 4135−4150.

(68) Jun, H.; Fabienne, T.; Florent, M.; Coulon, P. -E.; Nicolas, M.; Olivier, S. *Langmuir* **2012**, *28*, 15966−15974.

(69) Tsunoyama, H.; Ichikuni, N.; Tsukuda, T. *Langmuir* **2008**, *24*, 11327−11330.

(70) Liu, D. X.; Liu, Z. C.; Chen, C.; Yang, A. J.; Li, D.; Rong, M. Z.; Chen, H. L.; Kong, M. G. *Sci. Rep.* **2016**, *6*, 23737.

(71) Tian, W.; Kushner, M. J. *J. Phys. D: Appl. Phys.* **2014**, *47*, 165201.

(72) Liu, D. X.; Bruggeman, P.; Iza, F.; Rong, M. Z.; Kong, M. G. *Plasma Sources Sci. Technol.* **2010**, *19*, 025018.

(73) Ding, K.; Lieberman, M. A.; Lichtenberg, A. J. *J. Phys. D: Appl. Phys.* **2014**, *47*, 305203.

(74) Vasko, C. A.; Liu, D. X.; Van Veldhuizen, E. M.; Iza, F.; Bruggeman, P. J. *Plasma Chem. Plasma Process.* **2014**, *34*, 1081−1099.

(75) Winter, J.; Tresp, H.; Hammer, M. U.; Iseni, S.; Kupsch, S.; Schmidt-Bleker, A.; Wende, K.; Dünnbier, M.; Masur, K.; Weltmann, K. -.; Reuter, S. *J. Phys. D: Appl. Phys.* **2014**, *47*, 285401.

(76) Askari, S.; Levchenko, I.; Ostrikov, K.; Maguire, P.; Mariotti, D. *Appl. Phys. Lett.* **2014**, *104*, 163103.

(77) Patacchini, L.; Hutchinson, I. H. *Phys. Plasmas* **2009**, *16*, 062101.

(78) Turi, L.; Rossky, P. J. *Chem. Rev.* **2012**, *112*, 5641−5674.

(79) Garrett, B. C.; Dixon, D. A.; Camaioni, D. M.; Chipman, D. M.; Johnson, M. A.; Jonah, C. D.; Kimmel, G. A.; Miller, J. H.; Rescigno, T. N.; Rossky, P. J.; Xantheas, S. S.; Colson, S. D.; Laufer, A. H.; Ray, D.; Barbara, P. F.; Bartels, D. M.; Becker, K. H.; Bowen, K. H., Jr.; Bradforth, S. E.; Carmichael, I.; Coe, J. V.; Corrales, L. R.; Cowin, J. P.; Dupuis, M.; Eisenthal, K. B.; Franz, J. A.; Gutowski, M. S.; Jordan, K. D.; Kay, B. D.; LaVerne, J. A.; Lymar, S. V.; Madey, T. E.; McCurdy, C. W.; Meisel, D.; Mukamel, S.; Nilsson, A. R.; Orlando, T. M.; Petrik, N. G.; Pimblott, S. M.; Rustad, J. R.; Schenter, G. K.; Singer, S. J.; Tokmakoff, A.; Wang, L. -.; Wittig, C.; Zwier, T. S. *Chem. Rev.* **2005**, *109*, 355−390.

(80) Buxton, G. V.; Greenstock, C. L.; Helman, W. P.; Ross, A. B. *J. Phys. Chem. Ref. Data* **1988**, *17*, 513−886.

(81) Nikiforov, A. Y. *High Energy Chem.* **2008**, *42*, 235−239.

(82) Barnett, R. N.; Landman, U.; Cleveland, C. L.; Jortner, J. *Phys. Rev. Lett.* **1987**, *59*, 811−814.

(83) Landman, U.; Barnett, R. N.; Cleveland, C. L.; Scharf, D.; Jortner, J. *J. Phys. Chem.* **1987**, *91*, 4890−4899.

(84) West, A. H. C.; Yoder, B. L.; Luckhaus, D.; Saak, C.-M.; Doppelbauer, M.; Signorell, R. *J. Phys. Chem. Lett.* **2015**, *6*, 1487−1492.

(85) Uhlig, F.; Marsalek, O.; Jungwirth, P. *J. Phys. Chem. Lett.* **2013**, *4*, 338−343.

(86) Sagar, D. M.; Bain, C. D.; Verlet, J. R. R. *J. Am. Chem. Soc.* **2010**, *132*, 6917−6919.

(87) Siefermann, K. R.; Liu, Y.; Lugovoy, E.; Link, O.; Faubel, M.; Buck, U.; Winter, B.; Abel, B. *Nat. Chem.* **2010**, *2*, 274−279.

(88) Siefermann, K. R.; Abel, B. *Angew. Chem., Int. Ed.* **2011**, *50*, 5264−5272.

(89) Geldart, D. J. W.; Chýlek, P. *J. Quant. Spectrosc. Radiat. Transfer* **2001**, *70*, 697−708.

(90) Polte, J. *CrystEngComm* **2015**, *17*, 6809−6830.

(91) Bonn, M.; Nagata, Y.; Backus, E. H. G. *Angew. Chem., Int. Ed.* **2015**, *54*, 5560−5576.

(92) Harada, M.; Okamoto, K.; Terazima, M. *J. Colloid Interface Sci.* **2009**, *332*, 373−381.

(93) Ghandi, K.; Findlater, A. D.; Mahimwalla, Z.; MacNeil, C. S.; Awoonor-Williams, E.; Zahariev, F.; Gordon, M. S. *Nanoscale* **2015**, *7*, 11545−11551.

(94) Pronschinske, A.; Pedevilla, P.; Murphy, C. J.; Lewis, E. A.; Lucci, F. R.; Brown, G.; Pappas, G.; Michaelides, A.; Sykes, E. C. *Nat. Mater.* **2015**, *14*, 904−907.

(95) Schofield, J.; Reiff, S. C.; Pimblott, S. M.; LaVerne, J. A. *J. Nucl. Mater.* **2016**, *469*, 43−50.